Marquette University

e-Publications@Marquette

Biomedical Engineering Faculty Research and Publications

Biomedical Engineering, Department of

9-2017

A Spectral CT Method to Directly Estimate Basis Material Maps From Experimental Photon-Counting Data

Tal Gilat Schmidt
Marquette University, tal.gilat-schmidt@marquette.edu

Rina Foygel Barber
University of Chicago

Emil Y. Sidky
University of Chicago

Biomedical Engineering Faculty Research and Publications/College of Engineering

A Spectral CT Method to Directly Estimate Basis Material Maps from Experimental Photon-Counting Data

Taly Gilat Schmidt
Department of Biomedical Engineering, Marquette University and Medical College of Wisconsin, Milwaukee, WI
Rina Foygel Barber
Department of Statistics, The University of Chicago, Chicago, IL
Emil Y. Sidky
Department of Radiology, The University of Chicago, Chicago, IL

Abstract:

The proposed spectral CT method solves the constrained one-step spectral CT reconstruction (cOSSCIR) optimization problem to estimate basis material maps while modeling the nonlinear X-ray detection process and enforcing convex constraints on the basis map images. In order to apply the optimization-based reconstruction approach to experimental data, the presented method empirically estimates the effective energy-window spectra using a calibration procedure. The amplitudes of the estimated spectra were further optimized as part of

the reconstruction process to reduce ring artifacts. A validation approach was developed to select constraint parameters. The proposed spectral CT method was evaluated through simulations and experiments with a photon-counting detector. Basis material map images were successfully reconstructed using the presented empirical spectral modeling and cOSSCIR optimization approach. In simulations, the cOSSCIR approach accurately reconstructed the basis map images (<;1% error). In experiments, the proposed method estimated the low-density polyethylene region of the basis maps with 0.5% error in the PMMA image and 4% error in the aluminum image. For the Teflon region, the experimental results demonstrated 8% and 31% error in the PMMA and aluminum basis material maps, respectively, compared with -24% and 126% error without estimation of the effective energy window spectra, with residual errors likely due to insufficient modeling of detector effects. The cOSSCIR algorithm estimated the material decomposition angle to within 1.3 degree error, where, for reference, the difference in angle between PMMA and muscle tissue is 2.1 degrees. The joint estimation of spectral-response scaling coefficients and basis material maps was found to reduce ring artifacts in both a phantom and tissue specimen. The presented validation procedure demonstrated feasibility for the automated determination of algorithm constraint parameters.

SECTION I. Introduction

Photon-counting detectors can simultaneously acquire X-ray measurements at multiple energy windows [1]. From the spectral data, basis material map images can be reconstructed to quantify material composition and density [2].

One approach for generating basis material maps first decomposes the spectral projection data into basis sinograms that represent the path length through the selected basis materials [2]–[3][4]. From these basis sinograms, basis material map images can be reconstructed using conventional or iterative CT reconstruction techniques [5]–[6][7][8]. This 'two-step' method is susceptible to noise, due to instability of the decomposition step. A second approach performs the standard flat-field normalization and negative logarithm followed by conventional CT reconstruction of each energy-window measurement, resulting in images reconstructed at different effective energies. The reconstructed images are then combined to estimate the basis material map images [9], [10]. This method, while relatively simple, is susceptible to beam hardening effects. A third approach is to directly estimate the basis material maps from the energy-window measurements, for which several iterative algorithms have been proposed [11]–[12][13][14][15]. The direct inversion approach is challenging due to the ill-conditioned inversion and nonlinear polyenergetic X-ray measurement model.

We previously developed an optimization-based approach to directly estimate the basis material map images from the measured projection data (i.e., 'one-step' inversion). This optimization-based approach models the polyenergetic x-ray transmission, which causes the optimization problem to be nonconvex, while incorporating non-smooth, convex constraints to stabilize the reconstruction and potentially reduce noise and/or dose [16]. To our knowledge, this nonconvex, constrained optimization problem can only be solved by the mirrored convex-concave (MOCCA) optimization algorithm [17]. The one-step inversion approach was previously demonstrated using simulated data that assumed a photon-counting detector with ideal energy response [16].

In practice, photon-counting detectors are susceptible to numerous effects that degrade the energy response, leading to photons detected in the incorrect energy windows [1]. Modeling and compensating for these nonideal effects is an active area of photon-counting CT research [18]–[19][20]. Because of the complex factors affecting photon-counting detection, experimental studies are required to effectively evaluate reconstruction algorithms. Several iterative spectral CT reconstruction approaches have been recently investigated on experimental data, for example demonstrating the potential to reduce noise [8], [21], perform material decomposition [22], and improve contrast-to-noise ratio [23]. To our knowledge, this paper presents the first

experimental implementation of a spectral CT iterative algorithm that both models the nonlinear polyenergetic X-ray transmission while enforcing convex constraints on the basis maps.

The presented spectral CT method consists of: (1) empirical effective spectra estimation; (2) formulation of a constrained, non-convex optimization problem (cOSSCIR) that includes scaling of the estimated spectra; (3) solution by the MOCCA algorithm; and (4) validation procedure for determining constraint parameters. Steps 1, 2, and 4 represent novel approaches presented in this paper for the purpose of reconstructing experimental photon-counting data. Section II presents a brief overview of the cOSSCIR optimization problem, Section III describes the empirical methods for modeling the detector spectral response, and Section IV describes the employed constraints and the validation procedure for selecting constraint parameters. The simulation and experimental methods are presented in Sections V and VI, respectively, with results in Sections VII and VIII, followed by discussion (Section IX) and conclusions (Section X).

SECTION II. Constrained One-Step Spectral CT Image Reconstruction (cOSSCIR)

This section presents a brief overview of the constrained One-Step Spectral CT Image Reconstruction (cOSSCIR) optimization problem. A full derivation and pseudo-code can be found in our previous publications [16], [17].

Basis material decomposition is performed by expressing the energy-dependent linear attenuation coefficient for energy E and spatial location $\vec{r}$, $\mu(E, \vec{r})$, as a basis expansion [2]

$$\mu(E, \vec{r}) = \sum_m \mu_m(E) f_m(\vec{r}) \ (1)$$

where $\mu_m(E)$ is the mth basis function and $f_m(\vec{r})$ is the spatial map of the contribution of that basis function to the total X-ray attenuation. The basis coefficients, f_m, provide quantitative information about the composition and density of the imaged material.

The goal of the investigated algorithm is to reconstruct the basis material maps $f_m(\vec{r})$ from counts data measured at multiple energy windows. The continuous basis material maps, $f_m(\vec{r})$, can be discretized by a voxel representation where f_{km} is the value of the basis map for material m and at voxel k. Eq. 2 is the discretized nonlinear forward model assumed by the optimization problem in this work, expressing the expected number of counts $\hat{c}_{w\ell}$ detected for ray ℓ in energy window w as a function of the discretized basis material maps, f_{km}

$$\hat{c}_{w\ell} = N_{w\ell} \sum_i s_{w\ell i} \exp\left[-\sum_{mk} \mu_{mi} X_{\ell k} f_{km}\right] \ (2)$$

Here $N_{w\ell}$ is the number of photons detected for ray ℓ in energy window w in the absence of an object, and $s_{w\ell i}$ represents the fraction of photons at discretized energy interval i detected in energy window w for ray ℓ the absence of an object. The line integration of the discrete material maps is performed by multiplication with matrix X, where $X_{\ell k}$ is the length of intersection between ray ℓ and voxel k,

The reconstruction approach investigated in this work inverts Eq. 2 to directly estimate the basis material maps, f_{km}, from photon counts detected for ray ℓ in energy window w, $c_{w\ell}$. The basis material maps are estimated through the following constrained optimization

$$f^* = \arg\min_f \left\{ \sum_{w\ell} D_{\text{TPL}}\left(c_{w\ell}, \hat{c}_{w\ell}(f)\right) + \sum_i \delta(P_i) \right\}, \ (3)$$

where DTPL is the data discrepancy function that assumes transmission Poisson likelihood (TPL)

$$D_{\text{TPL}}(c, \hat{c}(f)) = \sum_{w\ell} \left[\hat{c}_{w\ell}(f) - c_{w\ell} - c_{w\ell} \log \left(\hat{c}_{w\ell}(f)/c_{w\ell} \right) \right]. \quad (4)$$

Indicator functions $\delta(P_i)$ enforce the convex constraints $f \in P_i$, and are defined as

$$\delta(P) = \begin{cases} 0 & f \in P, \\ \infty & f \notin P, \end{cases} \quad (5)$$

where the P_i are convex sets corresponding to the desired constraints.

Minimizing the TPL discrepancy is equivalent to maximizing the likelihood assuming that the counts data are Poisson distributed, which is the case for an ideal photon counting detector. In practice, nonideal effects such as charge sharing, K-escape, and pileup alter this distribution. Although these effects introduce inconsistencies with the Poisson model, the TPL can be a useful measure of data discrepancy because it gives more weight to the measurements with higher counts [16].

The mirrored convex-concave (MOCCA) was previously proposed to perform the optimization described in Eq. 3 [16], [17]. The algorithm uses a convex-concave generalization to the Chambolle-Pock algorithm to handle the non-convex data discrepancy term. The algorithm derivation and pseudo-code are available in previous publications [16], [17].

SECTION III. Modeling the Detector Spectral Response

The forward model described in Eq. 2 assumes prior knowledge of the spectrum for each acquired energy window w and ray ℓ given by $s_{w\ell i}$ across energies i. In a photon-counting detector with ideal spectral response, each channel records the number of photons detected above its energy threshold. The counts measured in consecutive channels can be subtracted to calculate the number of photons detected between two energy thresholds, which we refer to as an energy window. In an ideal photon-counting detector, the energy windows are discrete and non-overlapping, as plotted in Fig. 1.
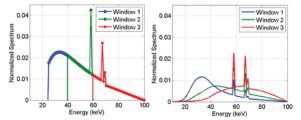

Fig. 1. (left) Ideal discrete spectra and (right) realistic spectra estimated from the experimental photon-counting CT system for energy windows with thresholds at 25 keV, 40 keV, and 60 keV.

In practice, numerous physical effects introduce errors in the number and energy of photons recorded by the detector [1]. One interpretation of these nonideal effects is that photons are detected in the incorrect discrete energy bins. Another interpretation is that these nonideal effects cause the energy windows to overlap, as photons with energy outside of the window thresholds contribute to the energy window measurement, as plotted in Fig. 1.

Nonideal detector effects can be incorporated into the optimization framework by including the effects in the data model (Eq. 2). Such models are under development for both flux-independent and flux-dependent effects [5], [18], [19]. One approach for modeling the flux-independent effects first measures the detector spectral response functions using monoenergetic measurements, for example using isotopes or synchrotron facilities [5]. The detector spectral response functions, $R(E, E')$, represent the probability of a photon with energy E being detected at energy E'. The effective spectrum for each energy window can be calculated by

integrating the energy response functions over E' for the range of energies between the comparator thresholds for that window. Including the spectral response functions in the forward data model was previously shown to reduce error in material decomposition estimates [5]. However, monoenergetic calibration measurements pose challenges for routine calibration, such as long acquisition times.

In this work, nonideal effects were incorporated into the reconstruction algorithm by empirically estimating the effective spectrum for each energy-window measurement and for each ray ($s_{w\ell i}$ in Eq. 2) using calibration transmission measurements, as will be described in Section VI-B. This approach should approximately account for the flux-independent detector effects. Pulse-pileup is not considered directly in this work, but could be incorporated in the future with the further development of pileup models.

Photon-counting CT images are also known to be susceptible to ring artifacts, due to variations in the energy thresholds and spectral response across detector pixels [5], [24], [25]. Despite these issues, the decomposed basis material map images should theoretically be immune to ring artifacts if the forward model (Eq. 2) completely describes the measurement process. In practice, the effective spectra estimated through calibration only approximately model the true detector response. Also, the spectral estimation is based on a limited combination of calibration materials. The resulting errors in material decomposition estimates obtained from projection data may vary across detector pixels due to varying detector response, leading to rings in the basis material map images that can be more severe than in the reconstructed energy-window images. Ring artifacts may also be introduced when the detector pixel spectral responses drift between the time of calibration and data acquisition, due to effects such as temperature.

We propose an empirical spectral-response scaling method to adjust, during reconstruction, the amplitude of the estimated effective spectra to further reduce the data discrepancy. The proposed scaling factors adjust the number of photons detected in each energy window for each detector pixel, which is an approximate correction for errors in the distribution of photon energies detected by each window.

The spectral-response scaling factor, a_{wp}, for window w and detector pixel p is incorporated into the cOSSCIR data model as

$$\hat{c}_{w\ell}(f, a) = N_{w\ell} \sum_i s_{w\ell i} \exp\left[-a_{wp_\ell} - \sum_{mk} \mu_{mi} X_{\ell k} f_{km}\right] \quad (6)$$

where p_ℓ is the detector pixel corresponding to ray ℓ. We assume that the scaling factor for each detector pixel is constant over the scan time such that the scaling factor depends only on the detector pixel. The vector of a_{wp} scaling factors are estimated jointly with the basis material maps using the MOCCA optimization algorithm

$$(f^*, a^*) = \arg\min_{f,a} \left\{ \sum_{w\ell} D_{\text{TPL}}\left(c_{w\ell}, \hat{c}_{w\ell}(f, a)\right) + \sum_i \delta(P_i) \right\}. \quad (7)$$

Application of the MOCCA algorithm to the new data model with spectral-response scaling in Eq. (6) is straightforward because a and f enter the model as a linear combination.

SECTION IV. Convex Constraints and Validation Procedure

A major advantage of our cOSSCIR optimization approach is that constraints can be readily incorporated to stabilize inversion of the data model. In this work, total variation (TV) constraints were placed on the basis material map images, and an ℓ_2-norm constraint on the spectral-response scaling factors.

The TV constraints were formulated as

$$\|f'_m\|_{\text{TV}} \equiv \||\nabla f'_m|\|_1 \leq \gamma_m,$$

where ∇ represents the finite-differencing approximation to the gradient, and we use $|\cdot|$ to represent a spatial magnitude operator so that $|\nabla f'_m|$ is the gradient magnitude image (GMI) of transformed material map m. Transformation of the basis material maps was introduced in our previous work to improve convergence of the one-step algorithm [16]. This μ-preconditioning step orthogonalizes the basis material attenuation functions.

For the cases where the spectral-response scaling factors a_{wp} were jointly estimated during reconstruction (Section III), an additional constraint was placed on the magnitude of the vector of scaling factors to control the strong linear dependence between the scaling coefficients and the basis material maps

$$\sqrt{\sum_{wp} (a_{wp})^2} \leq \alpha.$$

In the current application with two basis materials, such as PMMA and aluminum as used in this study, there are two TV constraint parameters, γ_m, and a spectral-response scaling constraint parameter, α. Determining the optimal settings of these parameters is a difficult task even by visual assessment, because obtaining basis maps at each setting of the three constraint parameters entails full iterative image reconstruction making a grid search impractical. The parameter tuning issue is even more acute when considering spectral CT for estimation tasks, as the quantitative values in the reconstructed basis material maps will vary with γ_m and α.

We investigated an automatic method of constraint parameter determination. One way to view constraints is that they prevent overfitting the available data. The measured counts data contain inconsistencies, due to both noise from random physical processes, and systematic error from unmodeled physics. In minimizing a data discrepancy term, the resulting basis material maps can become contaminated by these inconsistencies. Random noise can lead to the model over-fitting to the data if parameters are not constrained sufficiently.

We use a validation method to select constraint values to avoid this problem of over-fitting. The proposed validation method selects constraint parameters that minimize the TPL data discrepancy for data that was not used in the reconstruction of the basis images. More specifically, the validation method first randomly removes 10% of the data from the set of measurements across all detector pixels, projection angles, energy windows to serve as a "testing" dataset. For a particular set of constraint parameters, the basis images are then reconstructed from the remaining 90% of the data, the "training" set. From the reconstructed basis images and estimated scaling factors the TPL data discrepancy was calculated for the testing set. By repeating this method with different constraint parameters, the parameters were optimized to be the values that minimized the testing TPL data discrepancy. Once the validated constraint parameters were obtained, reconstruction was performed using all counts data.

In order to perform the validation optimization, we employed constrained optimization by linear approximation (COBYLA) [26]. This algorithm is a standard small-scale solver that avoids the use of numerical differentiation in deriving descent steps. This is necessary because the testing TPL data discrepancy is effectively a non-smooth function of the constraint parameters, as objective values result from numerical solution of the cOSSCIR optimization problem. In our implementation, the MOCCA algorithm was run for 2000 iterations and the obtained solutions were checked against the TV and spectral-response scaling constraints. It was observed that each of the constraints were active and the computed TV and spectrum scaling vector norm agreed with the constraint parameters to better than 0.01% for all computations.

Care must be taken in selecting the initial values of the constraint parameters so as to minimize the number of COBYLA iterations necessary. Also, it is helpful to include scaling factors so that the parameter values are all of comparable magnitude. In order to properly initialize the COBYLA algorithm, we found it helpful to do two

coarse grid searches. First, we performed a one-dimensional grid search on the testing TPL using only the spectral-response scaling constraint. Second, we performed a two-dimensional grid search varying the basis material map TV constraints without use of spectral-response scaling, i.e. $a_{wp} = 0$. Using the results of these grid searches, it was possible to initialize the COBYLA algorithm so that the testing TPL was minimized within 50 iterations.

SECTION V. Simulation Study Methods

The simulations were designed to validate the novel algorithmic components presented in this paper: the joint estimation of spectral-response scaling factors with the basis maps, and the validation technique to select constraint parameters. An extensive simulation study of the cOSSCIR approach was previously published [16].

A. Image Reconstruction at Ideal Constraint Parameter Settings

A simulation study was performed to establish that, under relatively ideal conditions, the image reconstruction with spectral-response scaling using cOSSCIR provides accurate results.

We designed a computer simulation, shown in Fig. 2, of the experimental rod phantom shown in Fig. 3. The simulation was designed such that spectral-response scaling and Poisson noise were the only sources of data inconsistency. As such, the discretization of the voxelized phantom matched that of the reconstructed images. The materials in the rod phantom were modeled and the NIST values [27] for energy dependent attenuation data were used to generate mean counts data as specified in Eq. (6). The simulated energy window spectra were equal to spectra obtained experimentally as will be described in in Sec. VI-B. To simulate the detector pixel-to-pixel spectral variations found in the experimental data, a test vector of spectral-response scaling coefficients a_{wp} (also shown in Fig. 2) that resulted from experimental data were applied to the simulated spectra. By using the experimentally measured spectra, we modeled realistic variation across the detector pixels and absolute count values that allowed generation of Poisson noise that closely modeled the experiment.
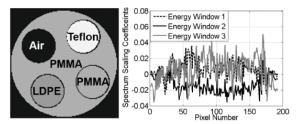

Fig. 2. (left) Simulated rod phantom that modeled the physical phantom used in the experiments. (right) Spectrum scaling coefficients (a_{wp}) modeled in the simulations. The coefficient values were based on those estimated in the experimental study.
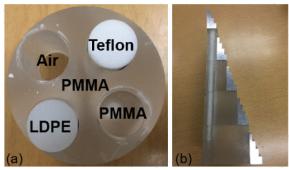

Fig. 3. (a) Rod phantom for quantifying material decomposition performance. The phantom diameter was 6.35-cm with 1-cm diameter rod inserts. (b) Step wedge phantom for spectral calibration consisting of PMMA (0-4 slabs of 2.54-cm thickness) and aluminum (0-4 slabs of 0.635-cm thickness).

The simulated data were reconstructed by the cOSSCIR approach into PMMA and aluminum basis material maps. During reconstruction, cOSSCIR assumed the same baseline energy-window spectra, s_{wli}, as the simulations, however the reconstruction algorithm did not have knowledge of the spectral-response scaling factors, a_{wp}, that were modeled during simulation. This simulation design validates that cOSSCIR algorithm produces accurate decomposition results while estimating the spectral-response scaling factors. One advantage of the constrained optimization framework is that, for simulation studies, ideal constraint values can be determined from the ground-truth software phantom. During cOSSCIR reconstruction of the simulated data, the constraint parameters were set to their respective phantom values

$$
\alpha = \alpha^{(\text{phantom})},
$$
$$
\gamma_{\text{aluminum}} = \gamma_{\text{aluminum}}^{(\text{phantom})},
$$
$$
\gamma_{\text{PMMA}} = \gamma_{\text{PMMA}}^{(\text{phantom})}.
$$

Because the cOSSCIR optimization is actually performed on transformed basis maps, we also tested use of the TV constraints on the transformed maps

$$
\alpha = \alpha^{(\text{phantom})},
$$
$$
\gamma_1 = \gamma_1^{(\text{phantom})},
$$
$$
\gamma_2 = \gamma_2^{(\text{phantom})},
$$

where numerical indices are employed because they are applied to the transformed basis material maps. The transformed basis maps do not have physical meaning as the orthogonalized basis attenuation functions can have negative values.

B. Testing the Use of Validation for Parameter Selection

The other novel aspect of the proposed framework is the use of validation to arrive at useful values of the constraint parameters. Simulations were performed to evaluate that the proposed validation technique can arrive at reasonable values for the spectral-response scaling and basis map TV constraint parameters. For this same simulation of the rod phantom we determined optimal values of the constraint parameters using the validation procedure described in Sec. IV. These constraint values were then applied to a cOSSCIR reconstruction using 100% of the spectral CT data.

SECTION VI. Experimental Study Methods

A. Spectral CT Acquisition

The bench-top system consisted of a microfocus X-ray tube (L9181-02, Hamamatsu, Shizouka, Japan) and a CdZnTe detector (NEXIS, Nova R & D, Riverside, CA) with two rows of 128, 1 mm pixels with five user-defined energy thresholds per detector pixel. This study used data from one detector row. Acquisitions were performed at 100 kV, 2-mm aluminum filtration, and with a raw-beam flux of 1.08×10^5 counts/(s · mm²) compared to a maximum detector count rate of 2×10^6 counts/(s · mm²). The source-to-detector distance was 82 cm and the source-to-isocenter distance was 55 cm. CT data was acquired at 200 views per rotation, with 0.132 mAs per view. Spectral CT data was acquired at three energy windows, with threshold settings of 25 keV to 40 keV, 40 keV to 60 keV, and > 60 keV.

CT images were acquired of a 6.35-cm-diameter acrylic phantom (Fig. 3) with 1-cm-diameter rod inserts of acrylic, Teflon, low-density polyethylene (LDPE) and air. This phantom provided regions of known material composition for evaluating the bias of the decomposition algorithm. A chicken tissue specimen was also imaged to demonstrate the algorithm performance for a more complex object.

B. Spectral Models

The cOSSCIR optimization requires a model for the effective spectra of each energy window measurement. Reconstruction of PMMA and aluminum basis images was performed assuming an ideal detector response and the 100 kV spectrum with 2-mm aluminum filtration output by the Spec78 software [28] and sampled at 1 keV intervals between 10 keV and 100 keV. The ideal spectrum was divided into discrete energy windows with thresholds of 25 keV, 40 keV, and 60 keV, as plotted in Fig. 1. Performing a reconstruction with the ideal spectrum provides a reference for the amount of nonideality in the experimental data, which helps us evaluate the compensation provided by the spectral estimation method.

Another set of reconstructions was performed with effective spectra that were estimated using a previously proposed empirical method [29]. A step wedge phantom (Fig. 3b) was used to acquire 25 transmission measurements through all combinations of PMMA (0-4 slabs of 2.54-cm thickness) and aluminum (0-4 slabs of 0.635-cm thickness). Transmission measurements were performed at 0.6 mAs for each measurement and at the same incident flux as the CT acquisitions. The previously proposed Expectation-Maximization (EM) iterative algorithm [29] estimated the normalized, discretized spectra ($s_{w\ell i}$ in [Eq. 2](#)) from the set of calibration measurements for each spectral window and ray measurement. Reconstruction was performed using the empirically estimated spectra with and without the additional spectral-response scaling correction described in Section III.

C. Comparison Two-Step Decomposition and Reconstruction

The energy-window data were also reconstructed into PMMA and aluminum basis images using a two-step approach in which decomposition was performed in the projection domain, followed by filtered backprojection reconstruction of the basis images [5]. Both iterative and empirical methods have been proposed to perform this inversion in the projection domain [3], [5], [30]. An iterative maximum likelihood expectation (MLE) algorithm, based on a Poisson noise model, was implemented to estimate the basis map sinograms, as in previous work [3], [5]. The decomposition algorithm used the same empirically estimated spectra for each energy window and ray measurement, $s_{w\ell i}$, as in the cOSSCIR approach. The basis images were reconstructed from the estimated basis sinograms using fan-beam filtered backprojection reconstruction and the same reconstruction grid as the cOSSCIR algorithm. An additional decomposition and reconstruction was performed with the estimated spectra adjusted by the scaling factors output by the cOSSCIR optimization approach. The resulting basis map images provide a comparison to the cOSSCIR images, with both reconstructions assuming the same estimated spectra.

D. Evaluation Metrics

The mean value was calculated in 770-image-pixel regions of interest (ROIs) in the Teflon and LDPE region of the rod phantom in the reconstructed PMMA and aluminum basis material map images. Teflon and LDPE were used as test materials because they were not included in the empirical calibration. The ground-truth basis material coefficients were obtained from the NIST attenuation functions [27] and the measured density of the test materials. The percent error in the reconstructed basis material map images was calculated relative to the ground-truth coefficients. The standard deviation of the basis map values was calculated within each ROI and then normalized by the root mean square of the ROI, to account for the different orders of magnitude between the PMMA and aluminum basis map values. Because of potential negative basis map values, the root mean square of the ROI was used for normalization rather than the mean of the ROI.

Quantitative evaluation of the basis material map images does not provide a complete picture of the performance of material decomposition estimator. For example, the contribution of the two basis materials to the overall attenuation may be unequal. A small error in the estimated coefficient of a basis material with high contribution to the overall attenuation could be meaningful, while a large error in the estimated coefficient of a

basis material with small contribution may be negligible. Evaluating the noise standard deviation or ring artifact level in the two basis material map images separately can also be problematic, as the noise or ring artifacts may be correlated. Therefore, additional metrics were calculated to further evaluate the performance of the basis material image estimates.

For each image pixel in the reconstructed basis material maps, the two basis material coefficients resulting from decomposition define a vector in the two dimensional space spanned by the basis materials. The direction of this vector represents a unique material composition, while the magnitude of the vector is related to the material density. For each investigated reconstruction approach, the basis decomposition vector angle and magnitude were calculated and averaged within the rod ROIs.

The basis material map images were also linearly combined to form an image representing the monoenergetic linear attenuation coefficient at each image pixel, as described by

$$f_E(\vec{r}) = \mu_{\text{PMMA}}(E)f_{\text{PMMA}}(\vec{r}) + \mu_{\text{aluminum}}(E)f_{\text{aluminum}}(\vec{r}). \quad (8)$$

Using this method, the 25, 35, 45, 65, and 85-keV images were calculated for all of the investigated approaches using the NIST attenuation data from PMMA and aluminum [27]. The percent error and normalized standard deviation in the Teflon and LDPE ROIs of the monoenergetic images were calculated.

SECTION VII. Simulation Study Results

A. Image Reconstruction at Ideal Constraint Parameter Settings

Fig. 4 presents the results of the simulation study that assumed realistic energy window spectra and detector pixel-to-pixel variations while using the ideal constraint parameters. The error in the Teflon and LDPE regions of the PMMA map was less than or equal to 1% regardless of whether the TV constraint was applied to the original or transformed basis material maps. The error in the aluminum map was 0.4% (Teflon) and 0.5% (LDPE) when the TV constraints were applied to the the transformed basis material maps (i.e., μ preconditioning [16]), compared to 2% error (Teflon) and 5% error (LDPE) when the TV constraint was applied to the untransformed basis material maps, demonstrating a slight advantage when using the transformed basis material maps.
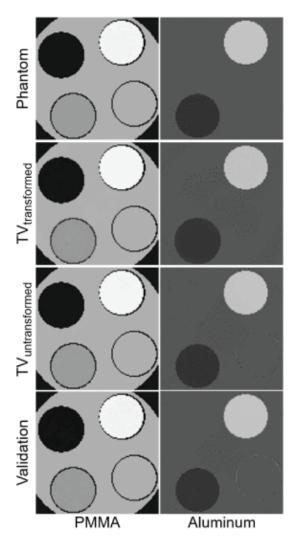
Fig. 4. Simulation results. PMMA and aluminum ground-truth basis maps for the voxelized phantom (Phantom) as well as basis maps reconstructed from simulated data using the ideal constraints applied to the basis maps ($TV_{Untransformed}$) and the transformed basis maps ($TV_{Transformed}$). Also displayed are basis maps reconstructed using constraints obtained through the presented validation procedure (Validation). The basis maps are unitless and are displayed at windows of [−0.1, 1.5] for the PMMA images and [−0.1, 0.2] for the aluminum images.

The benefit in employing the TV constraints for the transformed maps is seen in the convergence properties of cOSSCIR. The absolute difference between the TV values of the estimated maps and the true TV values are are shown in Fig. 5, where it is seen that the TV value for $f_{aluminum}$ is particularly slow to converge for the case where TV is applied directly to the basis material maps. Algorithm efficiency is of particular concern because we intend to perform searches over the constrained parameter space. As a result we choose to apply the TV constraints to the transformed basis material maps for all subsequent cOSSCIR reconstructions. This simulation study demonstrates that highly accurate image reconstruction and spectrum scaling estimation is possible under conditions where the only sources of data inconsistency are noise and effective spectra amplitude.
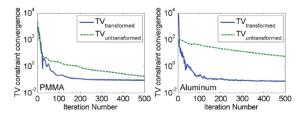
Fig. 5. Simulation results. Absolute difference between the TV values of the estimated maps and the true TV values plotted against iteration number for simulated data reconstructed with the TV constraint applied to transformed basis map images (i.e., μ preconditioning [16]) and with the TV constraint applied to the untransformed basis maps during reconstruction.

B. Testing the Use of Validation for Parameter Selection

When applied to the simulated data, the validation procedure arrived at constraint values that closely matched the actual phantom values; we observe that the ratios are all close to 1

$$
\begin{aligned}
\alpha^{(\text{valid})} &= 0.971\alpha^{(\text{phantom})}, \\
\gamma_1^{(\text{valid})} &= 0.932\gamma_1^{(\text{phantom})}, \\
\gamma_2^{(\text{valid})} &= 1.019\gamma_2^{(\text{phantom})}.
\end{aligned}
$$

The resulting images are shown in Fig. 4 The quantitative error in the basis map values was 0.3% for the PMMA map and −0.9% for the aluminum map in the Teflon region. In the LDPE region, the error was and 0.5% and 1.7% for the PMMA and aluminum map, respectively. These quantitative results demonstrate that the constraint values arrived at through validation perform nearly as well as the actual phantom values in terms of material map quantification. Also, the reconstructed images visually resemble the actual phantom.

SECTION VIII. Experimental Study Results

A. Rod Phantom Results

Fig. 6 displays the reconstructed PMMA basis, aluminum basis, and 45 keV monoenergetic images for the rod phantom. Images are displayed for the proposed method at the optimal constraint settings with spectral-response scaling (labeled as "cOSSCIR") and also for cOSSCIR reconstruction without spectral-response scaling (labeled as "TV only"). Fig. 6 also displays images that were reconstructed by a two step process of MLE decomposition into basis sinograms followed by filtered backprojection. MLE decomposition was performed using three different estimates for the spectra: assuming the energy window spectra estimated by the empirical calibration method (labeled as "Two-step"), the spectra adjusted by the spectral-response scaling coefficients estimated by the cOSSCIR algorithm (labeled as "Two-step adjusted"), and the discrete spectra expected for a detector with ideal energy response (labeled as "Two-step ideal spectra"), as plotted in Fig. 1. For reference, a ground-truth depiction of the phantom is presented.
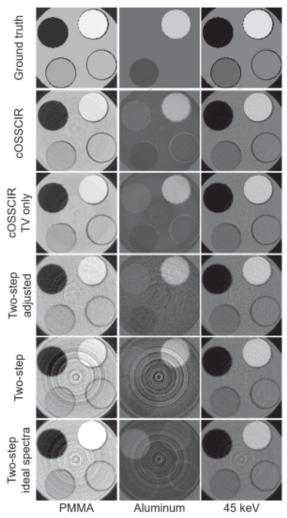
Fig. 6. Experimental results. PMMA and aluminum basis images reconstructed by the proposed method (labeled as "cOSSCIR"), cOSSCIR algorithm with only a TV constraint (i.e., no spectral-response scaling, labeled as "cOSSCIR TV only") and the two-step approach that assumed empirically estimated spectra (labeled as "Two-step"), estimated spectra with scaling correction (labeled as "Two-step adjusted"), and ideal spectra (labeled as "Two-step ideal spectra"). Images representing the 45 keV image are also displayed for each reconstruction approach. A ground-truth phantom image is also displayed. The display windows are [−0.1, 1.5] for the PMMA images, [−0.1, 0.2] for the aluminum images, and [0, 0.6] for the 45-keV image. The basis map values are unitless while the 45 keV images are in units of cm−1 .

Comparing the images in Fig. 6 reconstructed by cOSSCIR with only a TV constraint to the images reconstructed by the two-step method demonstrates considerable reduction in ring artifacts due to only the TV constraint in the cOSSCIR method. However, residual ring artifacts are visible in the cOSSCIR TV-only image, which were further reduced when the spectral-response scaling term was included in the cOSSCIR reconstruction. Ring artifacts were also reduced when the two-step method used the spectra adjusted by spectral-response scaling, suggesting that this scaling is effectively reducing ring artifacts.

Error in the image values, particularly in the aluminum basis images when compared to the ground-truth, can be seen in the images reconstructed by the two-step method assuming ideal spectra. For example, the background PMMA phantom region is zero in the ground-truth aluminum image but has negative value in the image reconstructed by the two-step method with ideal spectra. Also, the Teflon region is bright in the ground-truth aluminum basis image but is dark in the image reconstructed assuming ideal spectra. The images reconstructed

by the two-step method assuming ideal spectra demonstrate the nonideality present in the experimental energy window data. The use of empirically estimated spectra improved the qualitative agreement between the reconstructed and ground-truth images, although error can still be seen, for example negative values in the PMMA regions of the aluminum basis images.

The percent error and normalized standard deviation in the Teflon and LDPE regions of the phantom are plotted in Fig. 7 for the investigated reconstruction methods. The plots demonstrate that the −23% PMMA basis image error and 126% aluminum basis image error in the Teflon ROI obtained when assuming ideal spectra were reduced to 8% and 31% error, respectively, for the proposed cOSSCIR method. The two-step method resulted in error similar to cOSSCIR, with 10% and 30% error for the PMMA and aluminum basis image values, respectively. The use of the optimized spectral-response scaling parameter had a small effect (<5% difference) in the error for both the cOSSCIR and two-step approaches. Similar trends are seen in the LDPE results, with 0.5% error in the PMMA image and 4% error in the aluminum image for the cOSSCIR approach. The normalized standard deviation plotted in Fig. 7 quantifies the variation due to both noise and ring artifacts. Incorporating the scaled spectra that were determined by cOSSCIR into the two-step method reduced the normalized standard deviation in the Teflon region, with the cOSSCIR reconstructions providing the lowest normalized standard deviation.
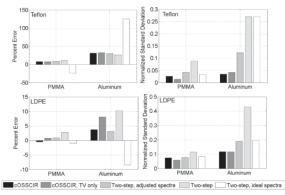

Fig. 7. Experimental results. (left) Percent error and (right) normalized standard deviation of image pixels within the (top) Teflon and (bottom) LDPE region of the aluminum and PMMA basis images.

Table I and II compare the angle and magnitude, respectively, of the material decomposition vectors in the two-dimensional space with the horizontal component of each vector representing the PMMA coefficient and vertical component representing the aluminum coefficient. The angle and magnitude are compared for the investigated reconstruction approaches in ROIs within the Teflon, LDPE, and PMMA rods. The angle of the vector represents the material composition, while the magnitude of the vector is related to the density. Figure 8 plots the estimated material decomposition vectors along an arc segment of the unit circle in the PMMA / aluminum space for the cOSSCIR reconstruction compared to ground truth. Visualizing the material decomposition vectors along the unit circle enables evaluating material decomposition accuracy independent of material density. The ground-truth vector for muscle is also presented to visualize how the error in decomposition angle for the proposed method compares to the difference in angle due to material composition.

TABLE I Comparison of the Angle of the Material Decomposition Vector in the PMMA and Aluminum Space, as Estimated in ROIs Within the Basis Material Maps. The Ground-Truth Angle is Also Presented, With all Angles in Units of Degrees

	Ground truth	cOSSCIR	Two-step adjusted spectra	Two-step ideal spectra
LDP E	-2.6	-2.4	-2.5	-2.8
PMM A	0	-1.3	-1.3	-2.3
Teflon	5.2	3.9	4.0	- I. I

	Ground truth	cOSSCIR	Two-step adjusted spectra	Two-step ideal spectra
LDPE	-2.6	-2.4	-2.5	-2.8
PMMA	0	-1.3	-1.3	-2.3
Teflon	5.2	3.9	4.0	-1.1

TABLE II Comparison of the Magnitude of the Material Decomposition Vector in the PMMA and Aluminum Space, as Estimated in ROIs Within the Basis Material Maps. The Ground-Truth Vector Magnitude is Also Presented

	Ground truth	cOSSCIR	Two-step adjusted spectra	Two-step ideal spectra
LOP E	0.9	0.9	0.8	0.9
PMMA	1.0	1.0	1.0	I. I
Teflon	1.4	1.3	1.3	1.8

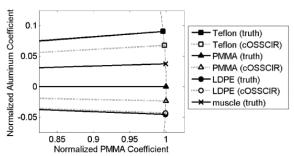|	Ground truth	cOSSCIR	Two-step adjusted spectra	Two-step ideal spectra
LDPE	0.9	0.9	0.8	0.9
PMMA	1.0	1.0	1.0	1.1
Teflon	1.4	1.3	1.3	1.8

Fig. 8. Unit vectors representing PMMA, LDPE, and Teflon materials in the PMMA and aluminum space as estimated by cOSSCIR compared to the ground-truth values. The dashed line represents the plotted arc segment of the unit circle. The ground-truth vector for muscle tissue is also plotted to visualize the separation between vectors due to changes in material composition.

Monoenergetic images reconstructed using the cOSSCIR algorithm (with optimized spectral-response scaling constraint) and the two-step algorithm (with scaled spectra) are displayed in Fig. 9 for a range of energy levels. The percent error and normalized standard deviation for the monoenergetic images are plotted in Fig. 10.
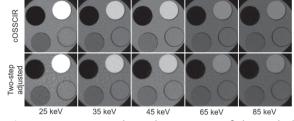

Fig. 9. Experimental results. Images of the rod phantom representing linear X-ray attenuation coefficients at 25, 35, 45, 65, 85 keV reconstructed by the cOSSCIR algorithm (with spectral-response scaling) and the two-step algorithm (with the scaled spectra). The display window is [0, 0.8] for all images, with the image values in units of cm^{-1}.
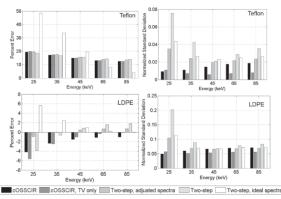
Fig. 10. Experimental results. (left) Percent error and (right) normalized standard deviation of image pixels in the (top) Teflon and (bottom) LDPE phantom regions for reconstructed monoenergetic images at 25, 35, 45, 65, 85 keV.

B. Tissue Specimen Results

Fig. 11 displays PMMA and aluminum basis images of the tissue specimen reconstructed by the proposed cOSSCIR method, cOSSCIR with only a TV constraint (no spectral-response scaling) and the two-step approach that assumed empirically estimated spectra with and without spectral-response scaling. Images representing the 45 keV image are also displayed for each reconstruction approach. The cOSSCIR images have reduced ring artifacts, with spectral-response scaling correction further reducing the ring artifacts. In Fig. 11, the fine structure in the soft tissue and bone regions are visualized in the aluminum images, in which adipose tissue has negative image pixel value. The negative image pixel values in the aluminum image are required to represent the linear attenuation coefficient function of adipose tissue because adipose tissue is outside the effective atomic number and density range spanned by the basis materials.
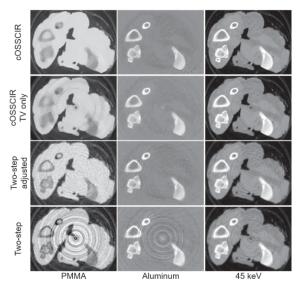

Fig. 11. Experimental results. PMMA and aluminum basis images of the tissue specimen reconstructed by the proposed cOSSCIR method, cOSSCIR with only a TV constraint (no spectral-response scaling) and the two-step approach that assumed empirically estimated spectra with and without scaling correction. Images representing the 45 keV image are also displayed for each reconstruction approach. The display windows are [−0.1, 0.1] for the PMMA images, [−0.3, 0.3] for the aluminum images, and [0, 0.4] for the 45-keV image. The basis map values are unitless while the 45 keV images are in units of cm^{-1}.

The TV constraint parameters control the tradeoff between denoising and retaining of fine structure. It is possible that fine anatomical structure can be lost as the TV constraint parameters decrease. Figure 12 displays regions of interest within the 45-keV monoenergetic image from cOSSCIR and the two-step method with adjusted spectra, to enable qualitative comparison of the visualization of fine structure. Fine structures of soft tissue surrounded by adipose tissue are depicted in the cOSSCIR images reconstructed using the optimized TV parameter settings. Fig. 13 displays the monoenergetic images at a range of energies resulting from the cOSSCIR and two-step approaches. Higher tissue contrast is visible at the lower energies. The cOSSCIR method resulted in less noise and artifacts at the low energies compared to the two-step approach.
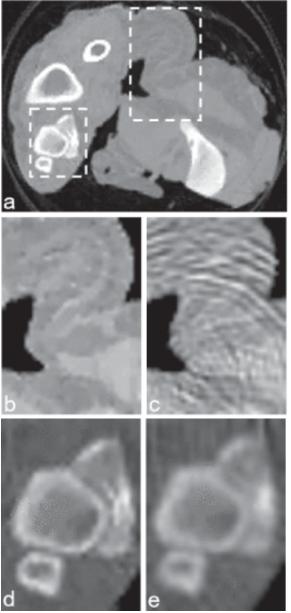

Fig. 12. (a) 45 keV image reconstructed by cOSSCIR depicting the two ROIs that are compared in the following subfigures. Soft tissue ROIs reconstructed by (b) cOSSCIR and (c) two-step method with adjusted spectra are displayed at window [0.1, 0.28]. Bone ROIs reconstructed by (d) cOSSCIR and (e) two-step method are displayed at window [0.1, 0.55].
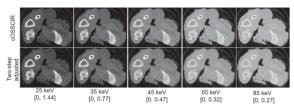
Fig. 13. Experimental results. Images of the tissue specimen phantom representing linear X-ray attenuation coefficients at 25, 35, 45, 65, 85 keV reconstructed by the cOSSCIR method (with spectral-response scaling) and the two-step algorithm (with the scaled spectra). The display window, listed for each energy level, was selected to span the range of values between air and the mid bone intensity. The image values are in units of cm^{-1}.

SECTION IX. Discussion

This study investigated the proposed spectral CT basis map estimation method through simulations and experiments. The simulation study, which modeled nonideal detector spectral response, demonstrated that the cOSSCIR optimization accurately reconstructed the basis maps when noise and effective spectra amplitude were the only sources of inconsistency between the forward and inverse models and when the ideal constraint values were employed. In simulations, the validation procedure determined the basis map TV and spectral-response scaling constraint parameters to within 7% of the true values. We do point out, however, that this particular simulation benefits from employing a test phantom where the basis material maps have a high degree of sparsity in the gradient-magnitude; this property makes the TV constraints extremely effective. Furthermore, it is known that there are many unmodeled physical processes in the presented simulations, particularly those that are associated with photon-counting detection. Simultaneous estimation of spectral-response scaling factors and basis material maps for spectral CT is an inverse problem that had not previously been studied, and the accurate results obtained by this simulation are encouraging.

The experimental study demonstrated reasonable decomposition results, with 0.5% error in the PMMA basis image and 4% error in the aluminum image for the LDPE region and 8% and 31% error in the Teflon region of the PMMA and aluminum basis images respectively, compared to −24% and 126% error when ideal spectra were assumed in the forward model. The lower error for LDPE compared to Teflon is likely because LDPE is more similar to the PMMA used for calibration. The cOSSCIR algorithm estimated the material decomposition angle to within 1.3 degree error, where, for reference, the difference in angle between PMMA and muscle tissue is 2.1 degrees. The error in the 65-keV monoenergetic image estimated with the proposed cOSSCIR approach was 1% for the LDPE region and 13% for the Teflon region. For comparison, a previous study using the same detector demonstrated 0.3% to 8% error in a Teflon region of the 70-keV mononergetic image using a two-step method with a neural network estimator and 1% to 16% error using a two-step method with empirical linearized MLE for decomposition [30].

The cOSSCIR and two-step approaches demonstrated similar quantitative decomposition results and similar error when using the same estimated spectra, suggesting that the quantitative accuracy depends primarily on the forward model as opposed to the inversion approach. The empirical spectral models used in this work reduced the decomposition error. However the relatively high residual error in the experimental results compared to the low error in the simulation results, suggests that the empirically estimated spectra did not sufficiently account for the physical effects within the detector. The forward model described in Eq. 2 does not include object scatter, which is another source of potential error in the decomposition results. Within the cOSSCIR framework, the forward model described in Eq. 2 can be modified in the future to more accurately model the acquisition physics, for example with detector-specific models [18], [19]. Additional sources of residual error may be uncertainties in the material properties of the calibration and test materials, as well as drift in the detector energy-window thresholds between calibration and CT acquisition.

The cOSSCIR optimization approach reduced the variation of the image pixel values within the reconstructed images compared to the two-step approach, where variation was due to both noise and ring artifacts. The spectral-response scaling term further reduced the normalized standard deviation in most cases. It would be preferable to address the source of ring artifacts directly, by designing detectors with improved uniformity and stability across detector pixels. While these efforts are underway, the proposed spectral-response scaling may be beneficial for reducing the residual ring artifacts that occur when performing material decomposition from projection data.

The investigated two-step approach used filtered backprojection for reconstruction, while the presented cOSSCIR implementation included TV constraints, which are known to reduce variation. Two-step reconstruction approaches with TV or other statistical-based regularization have been shown to reduce noise when reconstructing basis map images from decomposed sinograms [6], [8], [31].

The cOSSCIR approach presented in this paper is a general spectral CT optimization framework that specifies a data discrepancy function while allowing for convex constraints on the basis map images. In the specific implementation presented in this study, TPL was used as the data discrepancy, with TV constraints applied to the basis maps. The cOSSCIR approach, combined with the MOCCA algorithm, support the use of different data discrepancy and convex constraint functions in future implementations, including regularization that is not based on TV.

Regarding computational time of the cOSSCIR algorithm, we find it useful to report the number of iterations and the number of projection and back-projection operations per iteration, as these operations are the most time-consuming within the iterative loop. The actual execution time depends on implementation and computational platform. Within a validation run, we fixed the number of iterations for MOCCA to 2000. Only 90% of the data (the "training" data) are processed for image reconstruction. Within each loop, there are 3 projection and 3 back-projection operations. (There is an additional projection using the remaining 10% of the data, but this operation is negligible in comparison.) The COBYLA algorithm for optimizing the constraint parameters needed less than 100 iterations, where each iteration involves one call to MOCCA. After validation, we ran MOCCA on the final parameter settings for 5000 iterations using 100% of the data. We ran more iterations in the single run case in order to verify no significant change in going from 2000 to 5000 iterations. We emphasize that we have not attempted to improve efficiency of the full validation procedure. In future work, we will investigate, for example, the use of validation with inexact solution, where MOCCA is employed in a first pass with only 100 to 200 iterations.

These results are encouraging that validation may provide a useful means for constraint parameter determination. We note that some inaccuracy of the validation methodology can result from the numerical solver, in this case COBYLA, combined with inexact solution from cOSSCIR. Also, it is unknown whether the constraint values derived through the validation procedure represent the optimal choice in terms of visualization or quantitative estimation tasks.

SECTION X. Conclusion

Basis material map images were successfully reconstructed using the presented empirical spectral modeling and cOSSCIR reconstruction methods. The cOSSCIR optimization enabled modeling nonlinear polyenergetic X-ray transmission while enforcing convex constraints on the reconstructed basis material maps. The joint estimation of spectral-response scaling coefficients with the basis material maps, made possible by the cOSSCIR optimization framework, was found to reduce ring artifacts. The estimated effective spectra reduced decomposition error in the experimental study, although residual quantitative errors suggest the need for

improved modeling of detector effects. The presented validation procedure demonstrated feasibility for automated determination of algorithm constraint parameters.

ACKNOWLEDGMENTS

References

1. K. Taguchi, J. S. Iwanczyk, "Vision 20/20: Single photon counting X-ray detectors in medical imaging", *Med. Phys.*, vol. 40, no. 10, pp. 100901, 2013.

2. R. E. Alvarez, A. Macovski, "Energy-selective reconstructions in X-ray computerised tomography", *Phys. Med. Biol.*, vol. 21, no. 5, pp. 733-744, 1976.

3. E. Roessl, R. Proksa, "K-edge imaging in X-ray computed tomography using multi-bin photon counting detectors", *Phys. Med. Biol.*, vol. 52, no. 15, pp. 4679-4696, 2007.

4. D. Wu, L. Zhang, X. Zhu, X. Xu, S. Wang, "A weighted polynomial based material decomposition method for spectral X-ray CT imaging", *Phys. Med. Biol.*, vol. 61, no. 10, pp. 3749, 2016.

5. J. P. Schlomka et al., "Experimental feasibility of multi-energy photon-counting K-edge imaging in pre-clinical computed tomography", *Phys. Med. Biol.*, vol. 53, no. 15, pp. 4031-4047, 2008.

6. C. O. Schirra et al., "Statistical reconstruction of material decomposed data in spectral CT", *IEEE Trans. Med. Imag.*, vol. 32, no. 7, pp. 1249-1257, Jul. 2013.

7. R. Zhang, J.-B. Thibault, C. Bouman, K. D. Sauer, J. Hsieh, "Model-based iterative reconstruction for dual-energy X-ray CT using a joint quadratic likelihood model", *IEEE Trans. Med. Imag.*, vol. 33, no. 1, pp. 117-134, Jan. 2014.

8. A. Sawatsky, Q. Xu, C. O. Schirra, M. A. Anastasio, "Proximal ADMM for multi-channel image reconstruction in spectral X-ray CT", *IEEE Trans. Med. Imag.*, vol. 33, no. 8, pp. 1657-1668, Aug. 2014.

9. R. A. Brooks, "A quantitative theory of the Hounsfield unit and its application to dual energy scanning", *J. Comput. Assist. Tomograph.*, vol. 1, no. 4, pp. 487-493, 1977.

10. C. Maaß, M. Baer, M. Kachelrieß, "Image-based dual energy CT using optimized precorrection functions: A practical new approach of material decomposition in image domain", *Med. Phys.*, vol. 36, no. 8, pp. 3818-3829, 2009.

11. J. A. Fessler, I. A. Elbakri, P. Sukovic, N. H. Clinthorne, "Maximum-likelihood dual-energy tomographic image reconstruction", *Proc. SPIE*, vol. 4684, pp. 38-49, May 2002.

12. I. A. Elbakri, J. A. Fessler, "Statistical image reconstruction for polyenergetic X-ray computed tomography", *IEEE Trans. Med. Imag.*, vol. 21, no. 2, pp. 89-99, Feb. 2002.

13. C. Cai, T. Rodet, S. Legoupil, A. Mohammad-Djafari, "A full-spectral Bayesian reconstruction approach based on the material decomposition model applied in dual-energy computed tomography", *Med. Phys.*, vol. 40, no. 11, pp. 111916, 2013.

14. J. Chung, J. G. Nagy, I. Sechopoulos, "Numerical algorithms for polyenergetic digital breast tomosynthesis reconstruction", *SIAM J. Imag. Sci.*, vol. 3, no. 1, pp. 133-152, 2010.

15. Y. Long, J. A. Fessler, "Multi-material decomposition using statistical image reconstruction for spectral CT", *IEEE Trans. Med. Imag.*, vol. 33, no. 8, pp. 1614-1626, Aug. 2014.

16. R. F. Barber, E. Y. Sidky, T. G. Schmidt, X. Pan, "An algorithm for constrained one-step inversion of spectral CT data", *Phys. Med. Biol.*, vol. 61, no. 10, pp. 3784-3818, 2016.

17. R. F. Barber, E. Y. Sidky, "MOCCA: Mirrored convex/concave optimization for nonconvex composite functions", *J. Mach. Learn. Res.*, vol. 17, no. 1, pp. 5006-5056, 2016.

18. K. Taguchi, E. C. Frey, X. Wang, J. S. Iwanczyk, W. C. Barber, "An analytical model of the effects of pulse pileup on the energy spectrum recorded by energy resolved photon counting X-ray detectors", *Med. Phys.*, vol. 37, no. 8, pp. 3957-3969, 2010.

19. J. Cammin, J. Xu, W. C. Barber, J. S. Iwanczyk, N. E. Hartsough, K. Taguchi, "A cascaded model of spectral distortions due to spectral response effects and pulse pileup effects in a photon-counting X-ray detector for CT", *Med. Phys.*, vol. 41, no. 4, pp. 041905, 2014.

20. M. Touch, D. P. Clark, W. Barber, C. T. Badea, "A neural network-based method for spectral distortion correction in photon counting X-ray CT", *Phys. Med. Biol.*, vol. 61, no. 16, pp. 6132, 2016.

21. Z. Yu, S. Leng, Z. Li, C. H. McCollough, "Spectral prior image constrained compressed sensing (spectral PICCS) for photon-counting computed tomography", *Phys. Med. Biol.*, vol. 61, no. 18, pp. 6707, 2016.

22. J. Liu, H. Ding, S. Molloi, X. Zhang, H. Gao, "TICMR: Total image constrained material reconstruction via nonlocal total variation regularization for spectral CT", *IEEE Trans. Med. Imag.*, vol. 35, no. 12, pp. 2578-2586, Dec. 2016.

23. H. Ding, H. Gao, B. Zhao, H.-M. Cho, S. Molloi, "A high-resolution photon-counting breast CT system with tensor-framelet based iterative image reconstruction for radiation dose reduction", *Phys. Med. Biol.*, vol. 59, no. 20, pp. 6005, 2014.

24. X. Wang et al., "MicroCT with energy-resolved photon-counting detectors", *Phys. Med. Biol.*, vol. 56, no. 9, pp. 2791, 2011.

25. M. Persson, H. Bornefalk, "A framework for evaluating threshold variation compensation methods in photon counting spectral CT", *IEEE Trans. Med. Imag.*, vol. 31, no. 10, pp. 1861-1874, Oct. 2012.

26. M. J. D. Powell, "A direct search optimization method that models the objective and constraint functions by linear interpolation" in Advances in Optimization and Numerical Analysis, Dordrecht, The Netherlands:Springer, pp. 51-67, 1994.

27. M. Berger, J. Hubbell, S. Seltzer, J. Chang, J. Coursey, R. Sukumar, "XCOM: Photon cross sections database", *NIST Standard Reference Database*, vol. 8, no. 1, pp. 3587-3597, 1998.

28. K. Cranley, B. Gilmore, G. Fogarty, L. Desponds, "IPEM report 78: Catalogue of diagnostic X-ray spectra and other data", 1997.

29. E. Y. Sidky, L. Yu, X. Pan, Y. Zou, M. Vannier, "A robust method of X-ray source spectrum estimation from transmission measurements: Demonstrated on computer simulated scatter-free transmission data", *J. Appl. Phys.*, vol. 97, no. 12, pp. 124701, 2005.

30. K. C. Zimmerman, T. G. Schmidt, "Experimental comparison of empirical material decomposition methods for spectral CT", *Phys. Med. Biol.*, vol. 60, no. 8, pp. 3175, 2015.

31. Q. Xu, A. Sawatzky, M. A. Anastasio, C. O. Schirra, "Sparsity-regularized image reconstruction of decomposed K-edge data in spectral CT", *Phys. Med. Biol.*, vol. 59, no. 10, pp. N65, 2014.